On the Grinding Performance of Alumina Wheels in Ultrasonic Vibration-Assisted Grinding of Hardened GCr15 Steel

Yutong Qiu
Nanjing University of Aeronautics and Astronautics
Biao Zhao (zhaobiao@nuaa.edu.cn)
Nanjing University of Aeronautics and Astronautics https://orcid.org/0000-0002-8625-3935
Yang Cao
Nanjing University of Aeronautics and Astronautics
Wenfeng Ding
Nanjing University of Aeronautics and Astronautics
Yucan Fu
Nanjing University of Aeronautics and Astronautics
Changlan Pu
2Avic Cheng'du Aircraft Industrial (Group) Co. LTD

Research Article

Keywords: Wear behavior, WA wheel, Hardened GCr15 steel, Ultrasonic vibration-assisted grinding

Posted Date: November 30th, 2021

DOI: https://doi.org/10.21203/rs.3.rs-1094831/v1

Version of Record: A version of this preprint was published at The International Journal of Advanced Manufacturing Technology on February 14th, 2022. See the published version at https://doi.org/10.1007/s00170-022-08894-x.

Abstract

Composite manufacturing with multiple energy fields is an important source of processing technology innovation. In this work, comparative experiments on the conventional grinding (CG) and ultrasonic vibration-assisted grinding (UVAG) of hardened GCr15 steel were conducted with WA wheel. The grinding wheel wear patterns and chips were characterized. In addition, grinding force, force ratio, and ground surface quality were investigated to evaluate wheel performance. Results illustrate that the interaction between abrasive grains and workpiece in UVAG process has the characteristics of high frequency and discontinuity. The wear property of abrasive grains is changed and the grinding force is decreased because the generation of micro-fracture in abrasive grains improves the grinding wheel self-sharpening. Better surface quality is obtained, the surface roughness is reduced by up to 18.96%, and the number of defects on the machined surface is reduced through the superior reciprocating ironing of UVAG. Accordingly, WA wheel performance is improved by UVAG.

1. Introduction

In recent years, the demands of mechanical transmission systems have increased to meet the higher performance requirements (e.g., thrust-to-weight ratio, reliability, and service life) in modern aerospace, ship, and automobile industry sectors. The surface quality of gears, as the key components of the above mentioned transmission systems, plays a crucial influence on the service performance of whole systems [1–4]. At present, the grinding process is usually applied as the final procedure to raise the dimension accuracy and surface integrity of gears [5–7]. However, the gear steels, such as GCr15 steels, exhibit high hardness (reaching HRC 58-62), high tensile strength, and low thermal conductivity after the carburizing and quenching process; these characteristics are typical to difficult-to-cut materials [8–10]. In this case, the severe tool wear and poor ground surface quality are inevitable due to the lack of sufficient coolant in the grinding arc zone during the conventional grinding (CG) process [11–14]. Thus, improving the wear resistance of alumina wheels and coolant conditions inside the grinding arc zone is crucial in achieving desirable grinding performance and good machining quality.

Complex machining technology of ultrasonic vibration-assisted grinding (UVAG) has been the major approach for process improvement, and this multi-energy field composite manufacturing is an important source of machining technology innovation [15–17]. Consequently, this complex machining technology is usually used to improve the machining efficiency and surface integrity of difficult-to-cut materials at home and abroad. Bhaduri et al. [18, 19] conducted a comparison experiment to evaluate the ground surface roughness of TiAl intermetallic and Inconel 718 superalloy under CG and UVAG processes. They found that the grinding quality could be significantly improved due to the trajectory interference between abrasive grains by applying the ultrasonic vibrating method. Yu et al. [20] indicated that the polishing quality of Inconel 718 could be improved significantly under the changed motion state of the free abrasive particles because of ultrasonic vibration. The research by Nik et al. [21] proved that the application of UVAG method also contributed to reducing grinding forces and improving the surface quality of Ti-6Al-4V alloy grinding. Wei et al. [22] studied the material removal features of engineering

ceramics through a rotary UVAG process. The defect size was decreased remarkably using the ultrasonic vibration method, and thus, the ground surface quality could be improved. Furthermore, the cutting edges of abrasive grains tended to produce the macro-fracture and pull-out under the traditional grinding process, which led to the worse ground surface quality [23–25]. However, the influences of ultrasonic vibration on the material removal mechanism of grinding hardened steel and tool wear property were seldom analyzed.

Numerous researchers have investigated the tool wear behavior in the traditional grinding of difficult-to-cut materials to improve the ground surface quality by controlling the tool wear. For example, Li et al. [26] analyzed the grain wear evolution by acoustic emission (AE) testing. The results showed that abrasive wear is divided into three stages, and the wear state is gradually increasing. Xi et al. [27] compared and evaluated tool wear characteristics during grinding Ti_2AlNb, Ti-6Al-4V, and Inconel 718. The most severe tool wear could be observed in grinding of Ti_2AlNb intermetallics due to the strong affinity with SiC abrasives. Madopothula et al. [28] studied the grinding of AISI 52100 with two kinds of corundum grinding wheels. The results proved that SA abrasive grains were rubbed, which caused the main material to change from shearing to plough and friction. The abrasive fracture occurred when the WA wheel was grinding. Yang et al. [29] researched the form grinding of a 20CrMnTi steel tooth with a self-developed microcrystalline corundum wheel. The excellent self-sharpening of microcrystalline corundum abrasive increased the number of effective abrasive grains and reduced the extrusion and friction between the chip and the workpiece. In addition to improving ordinary abrasive grinding wheel, applying a multi-energy field processing method is also a way to reduce grinding wheel wear and improve grinding performance. Currently, the grinding wheel wear properties in UVAG for the controllability of UVAG process are still being explored.

Thus, this study conducts a comparative investigation on CG and UVAG to explore the effect of grinding parameters on wear evaluation and grinding performance for developing the UVAG strategy of hardened gear steel surface. Section 2 describes the experimental conditions and steps of ultrasonic vibration-assisted grinding of hardened GCr15 steel with WA wheel. Sections 3 and 4 indicate the analysis and conclusions, respectively.

2. Materials And Methods

2.1 Experimental procedures and materials

A precision surface grinding machine (BLOHM Profimat MT-408) coupled with coolant systems was used to perform grinding experiments, as shown in Fig. 1. The self-developed ultrasonic vibration system (Fig. 1b) was fixed to the workbench by support legs. The ultrasonic generator outputs high-frequency electrical signals, which are converted into mechanical vibration by the connected transducer and magnified by the horn. In the end, the workpiece attached to a titanium alloy platform connected to the horn could vibrate. The grinding wheel was white alumina (WA) wheels, as shown in Fig. 1c. The diameter of the grinding wheel d_s was 400 mm, and the axial width b_s was 20 mm. In addition, the abrasive grain

size of grinding wheels was about 160–200 μm. After each group of grinding experiment, a single point diamond dresser was used to dress the grinding wheel. The dressing parameters were as follows: grinding speed of v_c = 20 m/s, workpiece speed rate of f_c = 200 mm/min, and a total dressing depth of a_H = 0.2 mm. The detailed grinding process paraments are listed in Table 1. The material removal rate (MRR) Q'_w is expressed as Eq. (1):

$$Q_w^{'} = a_p \cdot v_w \quad (1)$$

The material removal volume (MRV) of the first pass in reciprocating grinding $V_{r1} = l_w \cdot b_w \cdot a_p$. Cumulative removal of workpiece material volume in each group of experiments was V_r = 450 mm^3.

The grinding force was collected by Kistler 9253B-type three-channel piezoelectric dynamometer, as shown in Fig. 1d. Then, it passed through the charge amplifier Kistler 5080A. Finally, it was measured on the software. The surface microstructure of grinding wheel, chips, and workpiece were characterized by Quanta 200 SEM, as shown in Fig. 1e. The machined surface roughness R_a was measured by MAHR M2 perthometer (cut length: 0.8 mm). Meanwhile, the ground surface profile was obtained by Sensofar S Neox 3D confocal microscopy. In this study, the ground materials were hardened GCr15 steel with a hardness of HRC60. The chemical composition content and mechanical properties of GCr15 are listed in Tables 2 and 3. Here, the workpiece with the dimension of 30 mm in length, 10 mm in width, and 12 mm in height were prepared. Then, the top surface of workpiece was firstly machined to the surface roughness of 0.8 μm before grinding experiments.

Table 1
Grinding process parameters.

Contents	Values
Machine tool	Blohm Profimat MT-408 surface grinder
Grinding mode	Reciprocating surface grinding
Abrasive wheel	WA wheel (mesh size of 80)
Ultrasonic frequency f (kHz)	19.6
Ultrasonic amplitude A (μm)	6
Wheel speed v_s (m/s)	25
Workpiece speed v_w (m/min)	Balance
Depth of cut a_p (μm)	10, 15, 20, 25
Material removal rate Q'_w ($mm^3/(mm·s)$)	1.33, 1.5, 2, 2.67, 3.33, 4.17
Cooling condition	5% emulsified water; 90 L/min, pressure at 1.5 MPa

Table 2
Chemical composition of GCr15.

Element	C	Si	Mn	P	S	Cr	Ni	Mo	Fe
Component/%	1.03	0.227	0.353	0.007	0.003	1.46	0.015	0.0096	Bal.

Table 3
Mechanical properties of GCr15.

Yield strength $\sigma_{0.2}$ (MPa)	Tensile strength σ_b (MPa)	Elastic modulus (GPa)	Density ρ (g/cm^3)	Thermal conductivity k (W/m·K)	Rockwell hardness (HRC)
1394	1748	210	7.81	46.6	60

2.2 Tangential ultrasonic vibrating method

In this work, tangential ultrasonic vibration-assisted was used for surface reciprocating grinding. The direction of high frequency vibration is parallel to the workpiece speed. The velocity of the grain in a cycle of reciprocating grinding can be presented as Eq. (2):

$$\begin{bmatrix} v_x \\ v_y \end{bmatrix} = \begin{bmatrix} (-1)^a \cdot v_w + v_s \cdot \cos\omega_s t + 2\pi f \cdot A\cos(2\pi f \cdot t + \varphi_0) \\ v_s \cdot \sin\omega_s t \end{bmatrix}, \begin{cases} a = 0, \text{down grinding} \\ a = 1, \text{up grinding} \end{cases}$$

2

where v_s, v_w, f, A, and t are the wheel speed, workpiece speed, ultrasonic frequency, ultrasonic amplitude, and time, respectively; ω_s is the angular velocity of the abrasive wheel, $v_s = \omega_s \cdot d_s$, d_s is the wheel radius; and φ_0 denotes the initial phase of ultrasonic vibration. A single abrasive trajectory of CG and tangential UVAG in the grinding arc is shown in Fig. 2a. This kind of grinding process has periodic reciprocating motion, which is like intermittent grinding. As shown in Fig. 2b, abrasive grain demonstrates the characteristic of separability during $t_1 - t_2$, and the workpiece is contacted again at t_3.

3. Results And Discussion

3.1 Grinding force and force ratio

Grinding force is a crucial parameter to characterize the grinding process, and it has an important effect on tool wear and machined surface quality [30, 31]. In order to achieve reliable data, the average value of three grinding force signals is selected as the grinding force value in the article. Graphs showing the grinding forces against MRR and MRV for the two grinding methods are detailed in Fig. 3.

As shown in Figs. 3a and 3b, the tangential grinding force F_t and the normal grinding force F_n of the two strategies exhibit a similar increasing trend with an increase in MRR. When the MRV of reciprocating grinding V_r = 450 mm^3 and the MRR increases from 1.33 $mm^3/(mm \cdot s)$ to 4.17 $mm^3/(mm \cdot s)$, the tangential grinding force of CG increases from 57.5 N to 169.2 N and the normal grinding force increases from 143.19 N to 381.73 N. Moreover, the tangential force of UVAG increases from 52.12 N to 144.42 N, and the normal force increases from 118.06 N to 322.77 N. A smaller grinding force under UVAG can be observed than that under CG. In UVAG, the maximum reductions in tangential force are 34.62%, 13.4%, and 14.66% with V_{r1}, V_r = 225 mm^3, and V_r = 450 mm^3, respectively; the maximum reductions in normal force are 34.25%, 17.08%, and 17.54% with V_{r1}, V_r = 225 mm^3, and V_r = 450 mm^3, respectively. Fig. 3c shows that the grinding force ratio F_n/F_t varies in the range of 2.06–2.49 and 2.02–2.32 with the increase in MRR in CG and UVAG, respectively. The WA wheel has an excellent grinding performance, and the small and stable grinding force ratio is due to that the grinding wheel has a good self-sharpening effect in UVAG. The tangential and normal grinding forces increase from 74 N and 162.52 N to 87.17 N and 179.71 N in CG, respectively. The tangential and normal grinding forces increase from 65.56 N and 134.43 N to 79.05 N and 162.6 N in UVAG, respectively. The normal grinding force has a steady and constant stage at MRV of 135 mm^3–315 mm^3 in UVAG. A different result is observed in CG, the normal grinding force keeps increasing.

In UVAG, material removal mechanism is changed because of the characteristic of separability. Due to the high-frequency interaction between active abrasive grains and workpiece surface, the cutting process is not continuous. This process of multiple-impact interaction makes the material begin to rollover more easily, and microcracks are formed in the grinding area, which will lead to effective material removal.

Therefore, the grinding force is decreased [32]. In a word, the application of ultrasonic vibration improves the grinding performance of workpiece material. However, the increase in MRR results in larger grinding loads [33], and the ultrasonic vibration effect on the grinding force reduction is reduced by the aggravated grinding wheel wear.

3.2 Wear surface topography

The grains on the grinding wheel are subjected to heavy load during the grinding process, and the effective life of the grains is an important affecting factor in the performance of the grinding wheel. Fig. 4 demonstrates the grinding wheel wear characteristics under the two grinding processes when grinding wheel speed v_s = 25 m/s and MRR = 2 $mm^3/(mm \cdot s)$. As shown in Figs. 4a–c, a mechanical clogging pore with a lot of chips is obvious in area Ⅰ under CG, and continuous chip adhesion can be observed on the surface of the abrasive grains in area Ⅱ. In addition, the wear patterns of grain pull-out and wear-flat can be easily formed. Conversely, the open pore is relatively clean and conducive to heat dissipation under UVAG, as shown in areas Ⅰ and Ⅱ in Figs. 4d–f. The chip adhesion is reduced, and the wear morphology of the abrasive grains exhibits microfracture. In this case, multiple cutting edges are generated, and the self-sharpening capability of grinding wheels can be effectively increased by UVAG processes.

In the grinding process, the typical wear of the grinding wheel is friction wear, abrasive fragmentation, and bond failure. Fig. 5a illustrates the force and thermal loads of a single abrasive grain. The wear patterns of grain under heavy load can be divided into brittle fracture and plastic wear. Grain wear behaviors of the grinding wheel for CG and UVAG are observed, as shown in Figs. 5b and c. Continuous friction wear is most commonly found in CG. Plastic wear occurs on the abrasive grain when the tangential force of abrasive grain F_{gt} exceeds the yield strength of abrasive materials in the cutting process. This wear is gradual, and the grain is eventually worn-flat. In addition, bond fracture and abrasive grain pull-out are observed when the shear force exceeds the bonding strength (Fig. 5b). Conversely, a random brittle fracture usually occurs in UVAG. Microcracks are generated due to the impact of contact between the white alumina grains and the workpiece material, and the microfracture of grain is formed by removing small fragments from the sliding surface (Fig. 5c). These mechanical wear behaviors of the grinding wheel are related to the grinding times, effective contact length, and grinding force. The impact times increase that the abrasive grain is subjected to intermittent loads during UVAG, which effectively reduces the friction wear. Moreover, the grinding wheel self-sharpening is realized by increasing the microfracture of grains.

3.3 Chip topography

Chip formation is an important issue in controlling the grinding wheel performance or the machined surface in the grinding process. The metal chip shapes obtained by grinding are flowing, blocky, ripping, shearing, and melting chips [34]. Fig. 6 shows the chip morphologies of CG and UVAG. Continuous chips

are observed. The surface of the chips close to the rake face is smooth, while the surface away from the rake face is rough. As shown in Figs. 6a–c, for CG processes, the width of the chips in the measurement area □ is 22 μm, and the length of the chips in the measurement area □ is 546 μm. As shown in Figs. 6d–e, the width and length of the chips in the measurement area □ for UVAG processes are 12 and 287 μm, respectively. Moreover, short C-type chips are generated in UVAG, as observed in area □ shown in Fig. 6f.

The chip generation behaviors of CG and UVAG are schematically illustrated in Fig. 7. The continuous chips generally appear in the condition of small cutting depth and high grinding speed in the grinding of plastic metal materials. Compared with UVAG, the cutting path of abrasive grain is continuous and stable in CG, and the chips are wider and longer. By contrast, the cutting trajectory has changed and a separation stage between the abrasive grain and the workpiece has existed. The corresponding continuous chips are broken into small chips with thinner and short structures in UVAG. In addition, the reduction in the maximum undeformed chip thickness in UVAG mentioned in Section 3.1 also reduces the chip size. In a sense, the chip breaking is realized by the separation characteristic of UVAG.

3.4 Surface quality

The surface quality significantly affects the performance of the parts and the reliability of the machine. The measurement direction of surface roughness R_a is perpendicular to the grinding infeed direction. The effects of MRR on R_a value in UVAG process are revealed in Fig. 8a. Surface roughness of two different grinding strategies have the same variation trend with the increased MRR. The R_a values are proportional to MRR. With the MRR increasing from 1.33 $mm^3/(mm·s)$ to 4.17 $mm^3/(mm·s)$ and grinding speed of v_s =25 m/s, the R_a value of CG and UVAG increases from 0.4 and 0.34 μm to 0.46 and 0.4 μm, respectively. Meanwhile, the R_a value is reduced by up to 18.96% in UVAG. Figs. 8b and 8c show the ground surface profiles obtained using the two types of grinding strategies in the case of Q'_w = 2 $mm^3/(mm·s)$. The peak-to-peak values for the height of grooves on the ground surface in CG and UVAG are from −1.440 and −1.146 μm to 1.504 and 1.204 μm, respectively. The R_a value is related to the height of the residual area of workpiece. By repeatedly ironing of the grinding wheel in UVAG, the tangential residual height of the workpiece surface is reduced. As a result, UVAG produces the better grinding quality compared to the other method [35].

SEM observation of the ground surface morphologies and surface damage during CG and UVAG is shown in Fig. 9. UVAG exhibits better ground surface quality than CG when MRR is fixed at 2 $mm^3/(mm·s)$. The various defect patterns with a larger area on the machined surface are clearly observed in CG. They appear as irregular areas, material fractures, voids, and redeposited material (Figs. 9a and 9b). Compared with CG, the machined surface presents excellent surface textures except for some grinding marks due to the cutting trajectory of the abrasive grain in UVAG (Figs. 9c and 9d).

The workpiece surface topography is the comprehensive effects result of the rubbing, ploughing, and cutting of abrasive grains on the workpiece. The material removal mechanism of a single abrasive was analyzed since the ground surface morphology characteristics of the workpiece. The abrasive grain is often considered to be a negative rake tool in the grinding process, and chips flow out from the rake face of abrasive grain. Fig. 10 shows the forming mechanism of the ground surface. For CG, the abrasive grain continuously contacts the workpiece, and the heat on the rake face increases because the coolant cannot enter the rake face. The workpiece material easily adheres to the surface of the grinding wheel, and then, redeposition occurs. In addition, the large-size wear debris mixed in the coolant is equivalent to free abrasive, which easily damages the ground surface as irregular area, fracture, void, and other characteristics. For UVAG, the size of wear debris is smaller, and the coolant flow field is changed by the separation of grain and workpiece, which can take much heat and abrasive fragments away in time. Therefore, the advantages of UVAG in intermittent grinding and reciprocating ironing can be used to reduce material damage, UVAG is beneficial to surface integrity.

4. Conclusions

In this work, ultrasonic vibration was applied to the grinding of hardened GCr15 steel to demonstrate the advantages of composite processing. The grinding behavior, including the grinding force and force ratio, wheel wear surface, and chip topography, as well as ground surface quality were discussed in detail. The following conclusions are obtained:

1. The material removal mechanism is changed by the separation characteristics of UVAG. Compared with CG, the grinding force is reduced and a stable grinding force ratio is obtained in UVAG. Moreover, the normal grinding force has a steady stage at MRV of 135–315 mm^3 during the reciprocating surface grinding with ultrasonic vibration.

2. The cutting process is discontinuous by the high-frequency action between abrasive grains and workpiece material in UVAG process. The phenomenon of chip clogging and adhesion is reduced, and the wear patterns of abrasive grains exhibit microfracture, which can effectively increase the self-sharpening capability of the grinding wheel.
3. The chip sizes in CG and UVAG differ. Small chips with thinner and short structures are observed in UVAG. In addition, the short C-type chips observed in the experiment also proved that chip breaking is effectively achieved by the separation characteristic of UVAG.
4. UVAG is beneficial to surface integrity. The surface roughness R_a is reduced with the feature of reciprocating ironing in UVAG. The coolant flow field is changed with the intermittent nature of UVAG, which can remove chips and grinding thermal in time, thereby reducing ground damage.

Declarations

Funding This work was financially supported by the National Natural Science Foundation of China (Nos. 51921003 and 52175415), Natural Science Foundation of Jiangsu Province (No. BK20210295), National

Key Laboratory of Science and Technology on Helicopter Transmission (Nanjing University of Aeronautics and Astronautics) (No. HTL-A-20G01), and the Foundation of Graduate Innovation Centre in NUAA (No. KFJJ20200506).

Competing interests The authors have no conflicts of interest to declare that they are relevant to the content of this article.

Availability of data and material All data generated or analyzed during this study are included in the present article.

Authors' contributions Yutong Qiu: experimentation, data curation, and writing the original draft. Biao Zhao: data collection and manuscript revision. Yang Cao: experimentation and methodology. Wenfeng Ding: supervision, conceptualization, and methodology. Yucan Fu: resources. Changlan Pu: funding acquisition.

Ethics approval and consent to participate The article follows the guidelines of the Committee on Publication Ethics (COPE) and involves no studies on human or animal subjects.

Consent to participate Not applicable.

Consent for publication Not applicable.

References

[1] Guo XZ, Shi ZY, Yu B, Zhao BY, Li K, Sun YQ (2020) 3D measurement of gears based on a line structured light sensor. *Precision Engineering* 61:160–169. https://doi.org/10.1016/j.precisioneng.2019.10.013

[2] Hu QC, Chen XB, Xu ZY, Mai QL, Zhu C (2020) Study on kinematic characteristics of planetary multistage face gears transmission. *Proceedings of the Institution of Mechanical Engineers, Part D: Journal of Automobile Engineering* 234:572–585. https://doi.org/10.1177/0954407019855908

[3] Waller MD, McIntyre SM, Koudela KL (2020) Composite materials for hybrid aerospace gears. *Journal of the American Helicopter Society* 65:1–11. https://doi.org/10.4050/JAHS.65.042010

[4] Li Q, Xie LY, Song JX, Li HY, Xu GL (2019) Research methods and applications of gear manufacturing process optimization. *Mathematical Problems in Engineering* 2019:1–17. https://doi.org/10.1155/2019/7043604

[5] Guerrini G, Lerra F, Fortunato A (2019) The effect of radial infeed on surface integrity in dry generating gear grinding for industrial production of automotive transmission gears. *Journal of Manufacturing Processes* 45:234–241. https://doi.org/10.1016/j.jmapro.2019.07.006

[6] Xiao YL, Wang SL, Ma C, Wang SB, Yi LL, Xia CJ, Dong JP (2021) Measurement and modeling methods of grinding-induced residual stress distribution of gear tooth flank. *International Journal of Advanced Manufacturing Technology* 115:3933–3944 https://doi.org/10.1007/s00170-021-07392-w

[7] Miao Q, Ding WF, Xu JH, Cao LJ, Wang HC, Yin Z, Dai CW, Kuang WJ (2021) Creep feed grinding induced gradient microstructures in the superficial layer of turbine blade root of single crystal nickel-based superalloy. *International Journal of Extreme Manufacturing* 3:045102. https://doi.org/10.1088/2631-7990/ac1e05

[8] Argoud V, Morel F, Pessard E, Bellett D, Thibault S, Gourdin S (2019) Fatigue behaviour of gear teeth made of case hardened steel: from competing mechanisms to lifetime variability. *Procedia Structural Integrity* 19:719–728. https://doi.org/10.1016/j.prostr.2019.12.078

[9] Li W, Liu BS (2018) Experimental investigation on the effect of shot peening on contact fatigue strength for carburized and quenched gears. *International Journal of Fatigue* 106:103–113. https://doi.org/10.1016/j.ijfatigue.2017.09.015

[10] Sales WF, Schoop J, da Silva LR, Machado ÁR, Jawahir IS (2020) A review of surface integrity in machining of hardened steels. *Journal of Manufacturing Processes* 58:136–162. https://doi.org/10.1016/j.jmapro.2020.07.040

[11] Wang WX, Salvatore F, Rech J, Li JY (2018) Comprehensive investigation on mechanisms of dry belt grinding on AISI 52100 hardened steel. *Tribology International* 121:310–320. https://doi.org/10.1016/j.triboint.2018.01.019

[12] Talon AG, Lopes JC, Tavares AB, Sato BK, Rodrigues AR, Genovez MC, Pinto TAD, de Mello HJ, Aguiar PR, Bianchi EC (2019) Effect of hardened steel grinding using aluminum oxide wheel under application of cutting fluid with corrosion inhibitors. *International Journal of Advanced Manufacturing Technology* 104:1437–1448. https://doi.org/10.1007/s00170-019-04005-5

[13] Gu SS, Yang CY, Fu YC, Ding WF, Huang DS (2014) Grinding force and specific energy in plunge grinding of 20CrMnTi with monolayer brazed CBN wheel. *Materials Science Forum* 770:34–38. https://doi.org/10.4028/www.scientific.net/MSF.770.34

[14] Huang XM, Zhou ZX, Ren YH, Mao C, Li W (2013) Experimental research material characteristics effect on white layers formation in grinding of hardened steel. *International Journal of Advanced Manufacturing Technology* 66:1555–1561. https://doi.org/10.1007/s00170-012-4439-y

[15] Wang JJ, Zhang JF, Feng PF, Guo P (2018) Experimental and theoretical investigation on critical cutting force in rotary ultrasonic drilling of brittle materials and composites. *International Journal of Mechanical Sciences* 135:555–564. https://doi.org/10.1016/j.ijmecsci.2017.11.042

[16] Cao Y, Zhu YJ, Ding WF, Qiu YT, Wang LF, Xu JH (2021) Vibration coupling effects and machining behavior of ultrasonic vibration plate device for creep-feed grinding of Inconel 718 nickel-based superalloy. *Chinese Journal of Aeronautics*. https://doi.org/10.1016/j.cja.2020.12.039

[17] Chen T, Ye ML, Liu SL, Tian SL (2017) Measurement of ultrasonic assisted grinding temperature based on fiber Bragg grating (FBG) sensor. *International Journal of Advanced Manufacturing Technology* 93:2561–2570. https://doi.org/10.1007/s00170-017-0721-3

[18] Bhaduri D, Soo SL, Aspinwall DK, Novovic D, Bohr S, Harden P, Webster JA (2017) Ultrasonic assisted creep feed grinding of gamma titanium aluminide using conventional and superabrasive wheels. *CIRP Annals* 66:341–344. https://doi.org/10.1016/j.cirp.2017.04.085

[19] Bhaduri D, Soo SL, Novovic D, Aspinwall DK, Harden P, Waterhouse C, Bohr S, Mathieson AC, Lucas M (2013) Ultrasonic assisted creep feed grinding of Inconel 718. *Procedia CIRP* 6:615–620. https://doi.org/10.1016/j.procir.2013.03.044

[20] Yu TB, Guo XP, Wang ZH, Xu PF, Zhao J (2019) Effects of the ultrasonic vibration field on polishing process of nickel-based alloy Inconel718. *Journal of Materials Processing Technology* 273:116228. https://doi.org/10.1016/j.jmatprotec.2019.05.009

[21] Nik MG, Movahhedy MR, Akbari J (2012) Ultrasonic-assisted grinding of Ti6Al4V alloy. *Procedia Cirp* 1:353–358. https://doi.org/10.1016/j.procir.2012.04.063

[22] Wei SL, Zhao H, Jing JT, Liu YF (2015) Investigation on surface micro-crack evaluation of engineering ceramics by rotary ultrasonic grinding machining. *International Journal of Advanced Manufacturing Technology* 81:483–492. https://doi.org/10.1007/s00170-015-7195-y

[23] Zhu YJ, Ding WF, Rao ZW, Zhao ZC (2019) Self-sharpening ability of monolayer brazed polycrystalline CBN grinding wheel during high-speed grinding. *Ceramics International* 45:24078–24089. https://doi.org/10.1016/j.ceramint.2019.08.115

[24] Naskar A, Choudhary A, Paul S (2020) Wear mechanism in high-speed superabrasive grinding of titanium alloy and its effect on surface integrity. *Wear* 462:203475. https://doi.org/10.1016/j.wear.2020.203475

[25] Zhao B, Ding WF, Xiao GD, Zhao JS, Li Z (2021) Effects of open pores on grinding performance of porous metal-bonded aggregated cBN wheels during grinding Ti–6Al–4V alloys. *Ceramics International*. https://doi.org/10.1016/j.ceramint.2021.08.004

[26] Li BK, Yin JF, Zhu YJ, Zhang X, Ding WF (2021) Grain wear evolution of cubic boron nitride abrasives during single grain grinding of powder metallurgy superalloy FGH96. *Ceramics International* 47:2508–2516. https://doi.org/10.1016/j.ceramint.2020.09.094

[27] Xi XX, Ding WF, Fu YC, Xu JH (2018) Grindability evaluation and tool wear during grinding of Ti_2AlNb intermetallics. *International Journal of Advanced Manufacturing Technology* 94:1441–1450. https://doi.org/10.1007/s00170-017-1005-7

[28] Madopothula U, Lakshmanan V, Nimmagadda RB (2017) Time dependent behavior of alumina grains manufactured by two different routes while grinding of AISI 52100 steels. *Archives of Civil and Mechanical Engineering* 17:400–409. https://doi.org/10.1016/j.acme.2016.11.004

[29] Yang LJ, Wang L, Liu Q, Tian XL (2018) Grinding performance of a new micro-crystalline corundum wheel when form-grinding automobile gears. *International Journal of Advanced Manufacturing Technology* 96:857–870. https://doi.org/10.1007/s00170-017-1514-4

[30] Li HN, Yu TB, Wang ZX, Li DZ, Wang WS (2017) Detailed modeling of cutting forces in grinding process considering variable stages of grain-workpiece micro interactions. *International Journal of Mechanical Sciences* 126:319–339. https://doi.org/10.1016/j.ijmecsci.2016.11.016

[31] Yu TY, Asplund DT, Bastawros AF, Chandra A (2016) Performance and modeling of paired polishing process. *International Journal of Machine Tools and Manufacture* 109:49–57. https://doi.org/10.1016/j.ijmachtools.2016.07.003

[32] Tawakoli T, Azarhoushang B (2008) Influence of ultrasonic vibrations on dry grinding of soft steel. *International Journal of Machine Tools and Manufacture* 48:1585–1591. https://doi.org/10.1016/j.ijmachtools.2008.05.010

[33] Miao Q, Ding WF, Kuang WJ, Yang CY (2020) Comparison on grindability and surface integrity in creep feed grinding of GH4169, K403, DZ408 and DD6 nickel-based superalloys. *Journal of Manufacturing Processes* 49:175–186. https://doi.org/10.1016/j.jmapro.2019.11.027

[34] Nadolny K, Kapłonek W (2016) The effect of wear phenomena of grinding wheels with sol-gel alumina on chip formation during internal cylindrical plunge grinding of 100Cr6 steel. *International Journal of Advanced Manufacturing Technology* 87:501–517. https://doi.org/10.1007/s00170-016-8500-0

[35] Isobe H, Hara K (2017) Visualization of fluctuations in internal stress distribution of workpiece during ultrasonic vibration-assisted cutting. *Precision Engineering* 48:331–337. https://doi.org/10.1016/j.precisioneng.2017.01.003

Figures

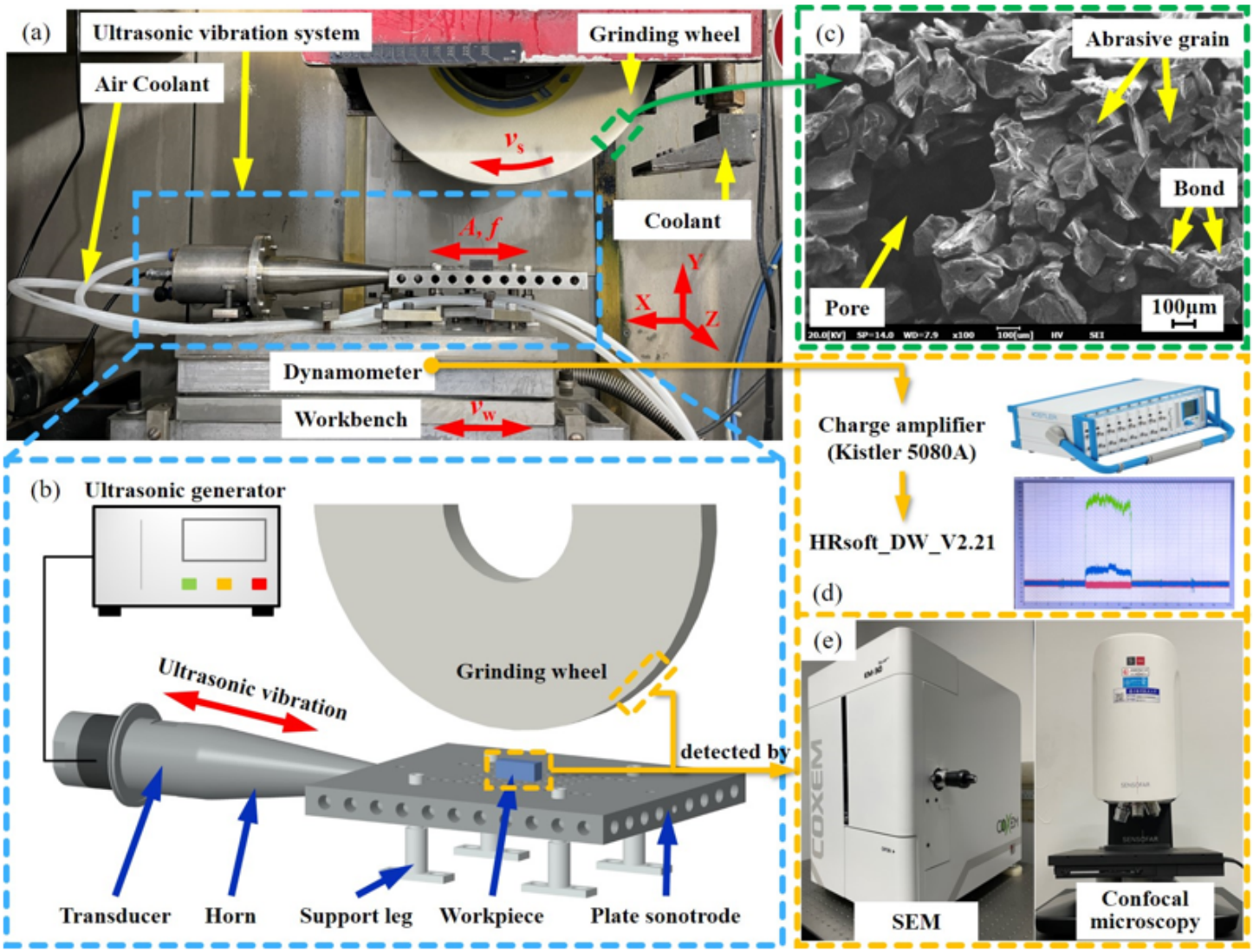

Figure 1

Reciprocating surface grinding experimental setup (a), including ultrasonic vibration system (b), WA wheel (c), grinding force measuring system (d), and surface measuring device (e).

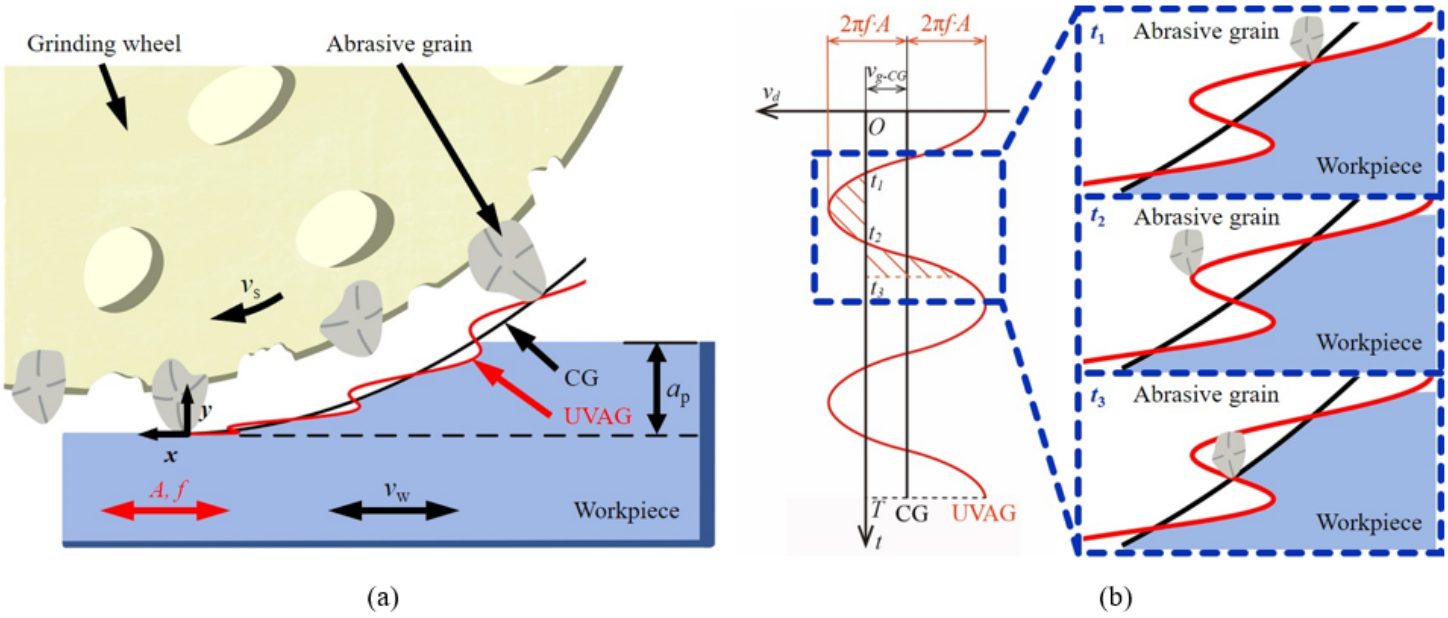

Figure 2

Schematic of (a) abrasive trajectory of CG and tangential UVAG, and (b) separation characteristics in UVAG process.

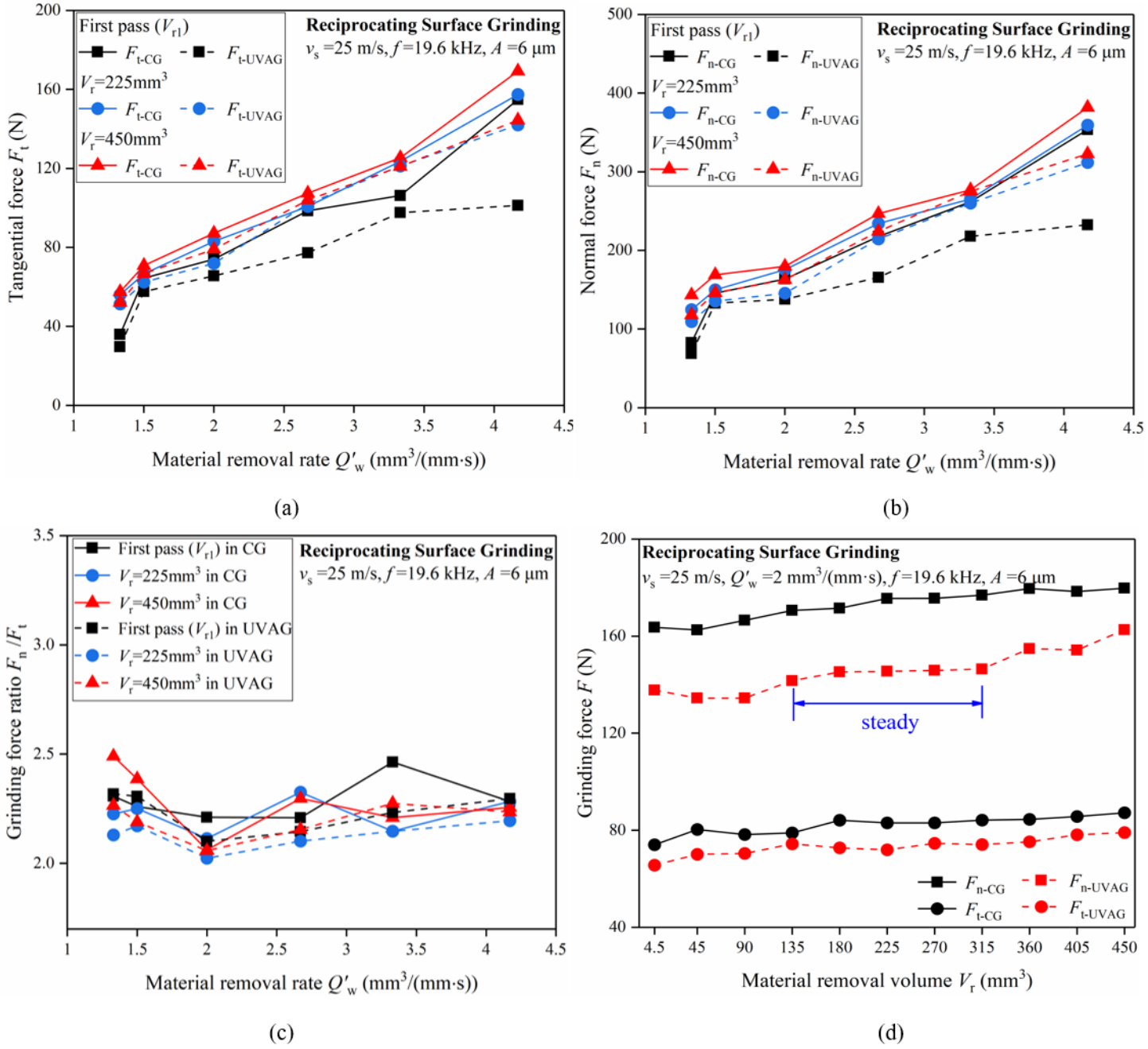

Figure 3

Effects of MRR on the (a) tangential force, (b) normal force, and (c) grinding force ratio for CG and UVAG, and (d) grinding force versus MRV in CG and UVAG.

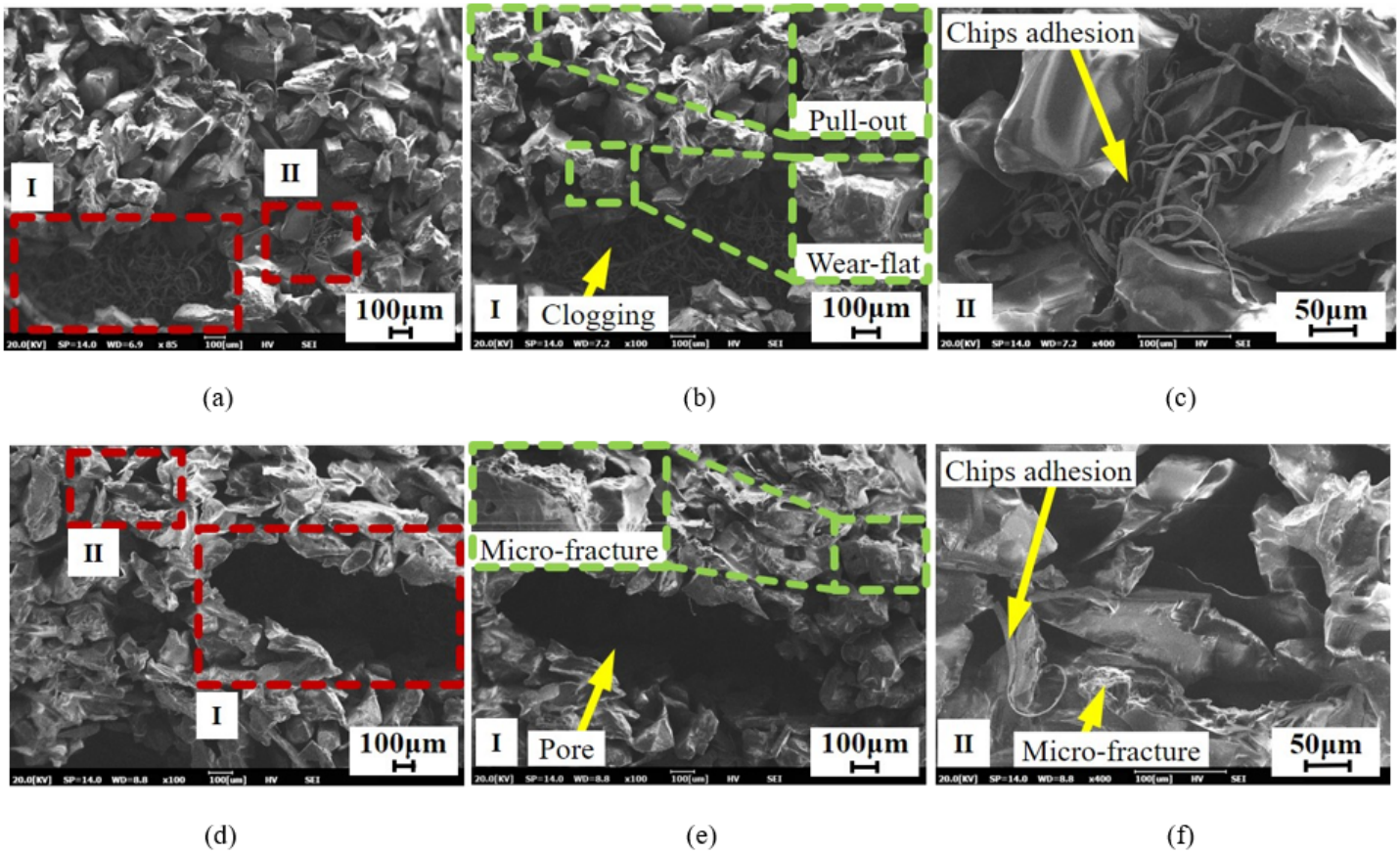

Figure 4

SEM microstructures of wheel surface of grinding wheels under CG (a) and UVAG (d), (b) and (e) magnified views of chip storage spaces and the characteristics of grain wear, (c) and (f) magnified views of chips adhesion.

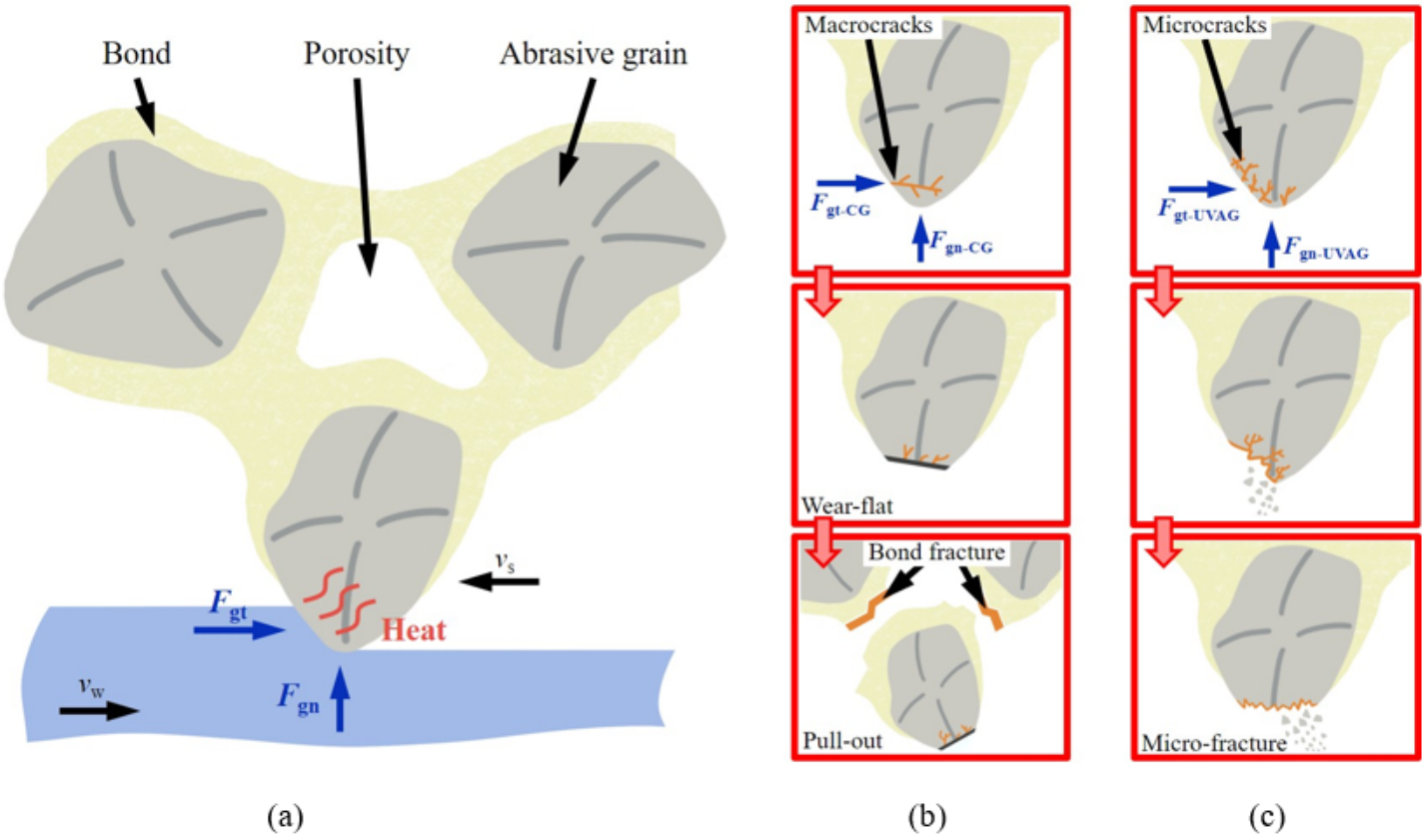

Figure 5

Schematic of (a) force load and thermal load of a single abrasive grain, and wear behaviors for CG (b) and UVAG (c).

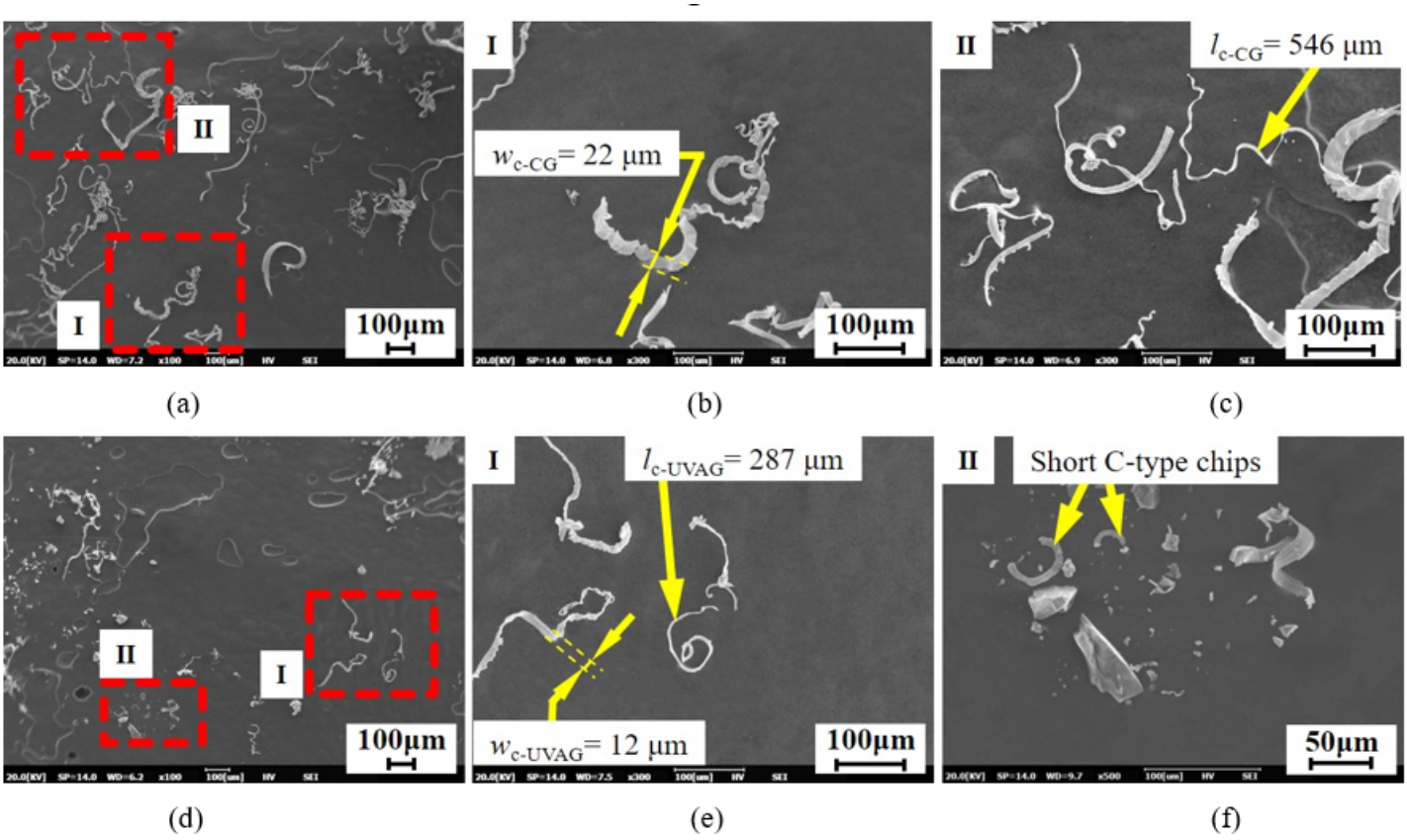

Figure 6

SEM microstructures of chip morphologies. In (a), two enlarged views of the red dashed frames indicate the width (b) and length (c) of the chips under CG, and in (d), two enlarged views of the red dashed frames indicate the size of the chips (e) and C-type chips (f) under UVAG.

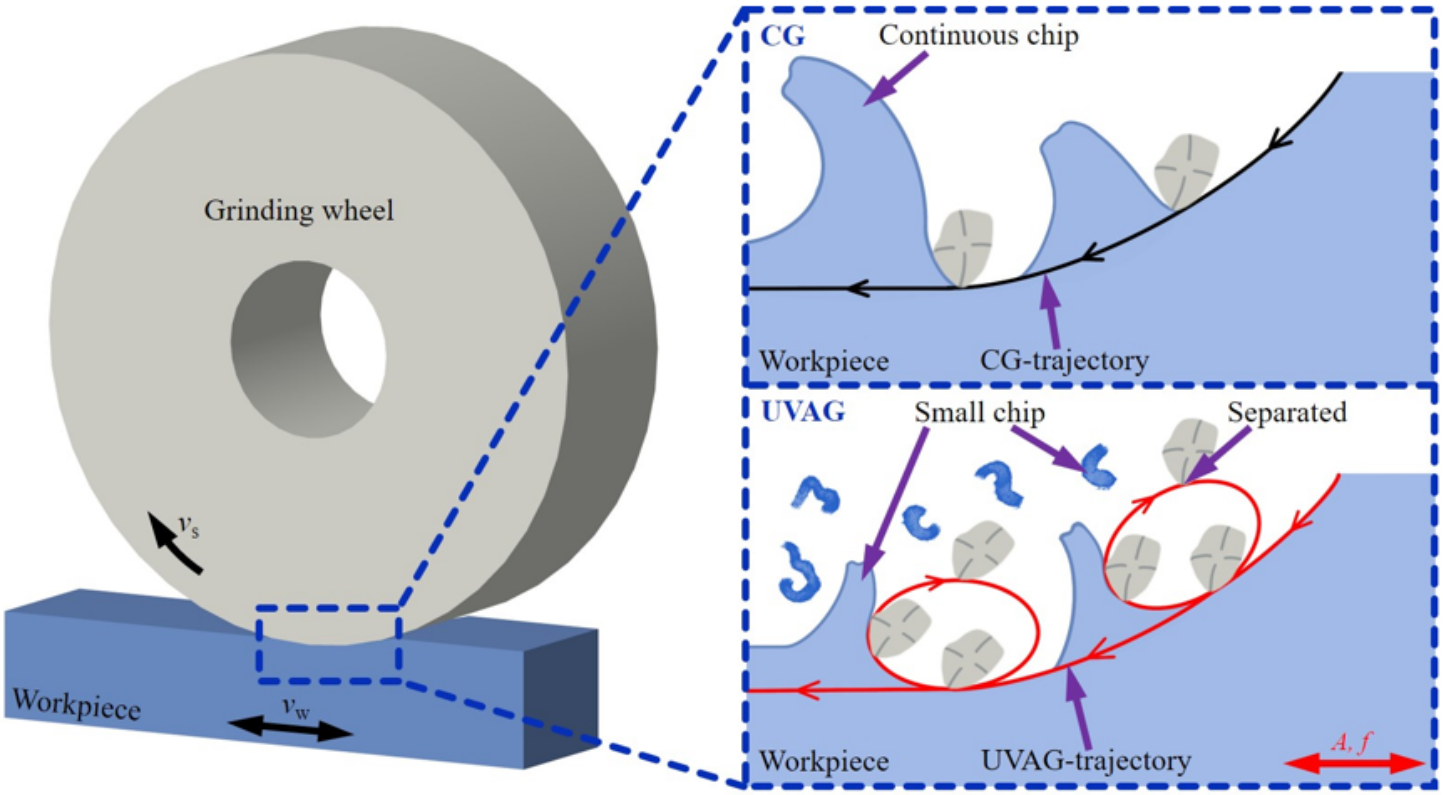

Figure 7

Schematic of chip generation behaviors of CG and UVAG.

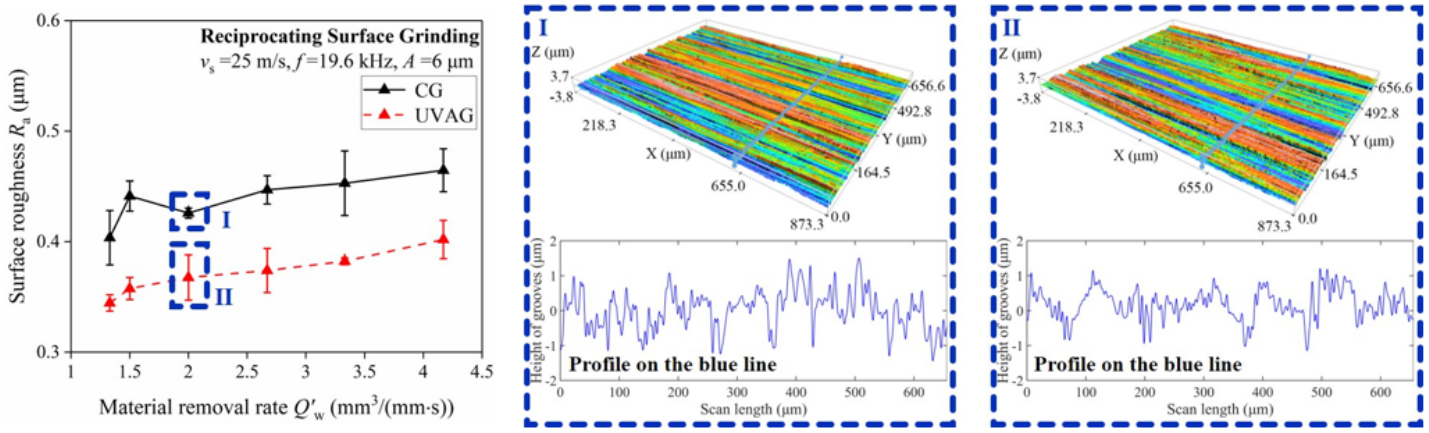

Figure 8

Ground surface roughness versus MRR in CG and UVAG (a), and ground surface profile produced by CG (b) and UVAG (c) with Q'w = 2 mm3/(mm·s).

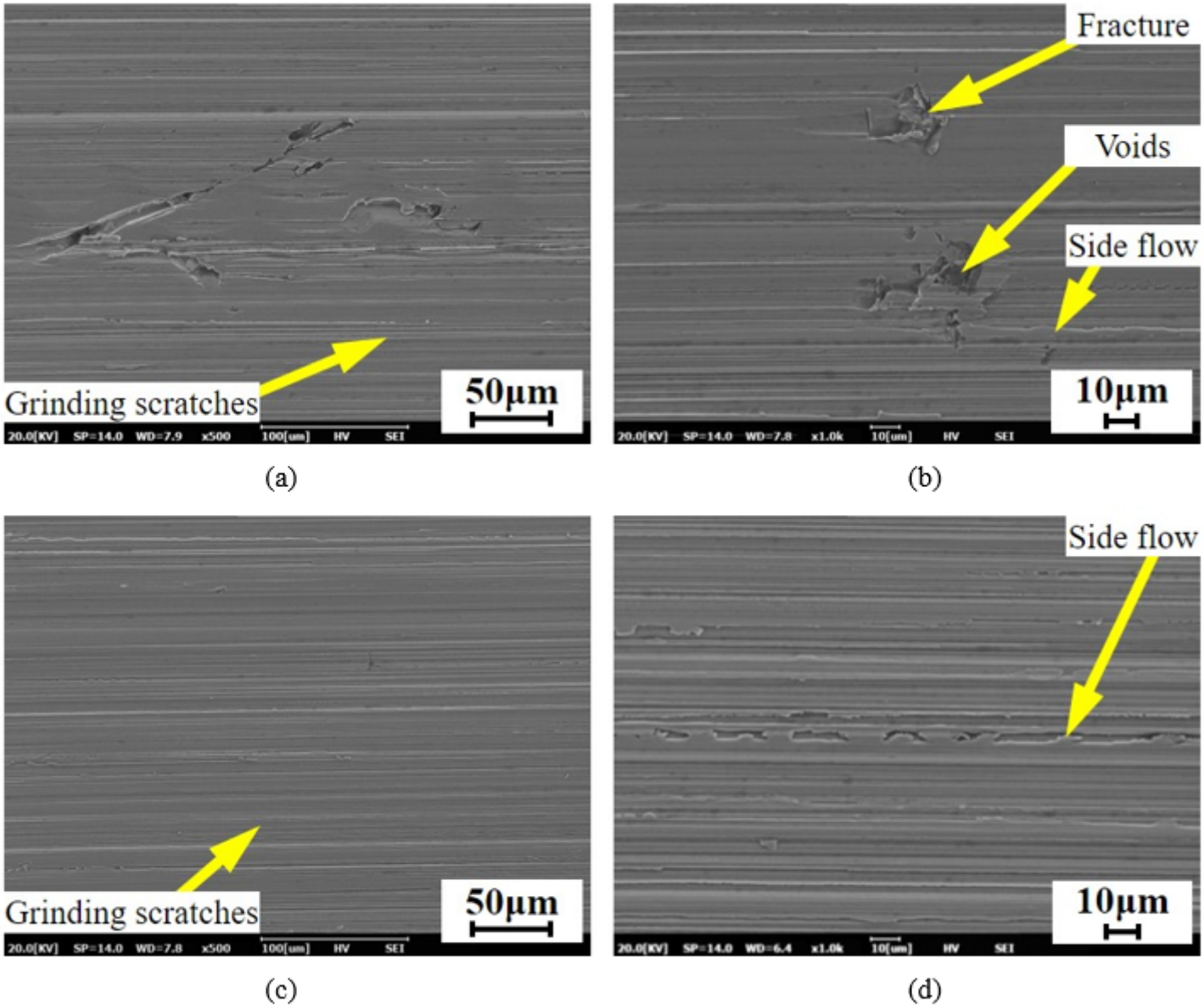

Figure 9

Ground surface morphologies during CG (a, b) and UVAG (c, d) with Q'w = 2 mm3/(mm·s).

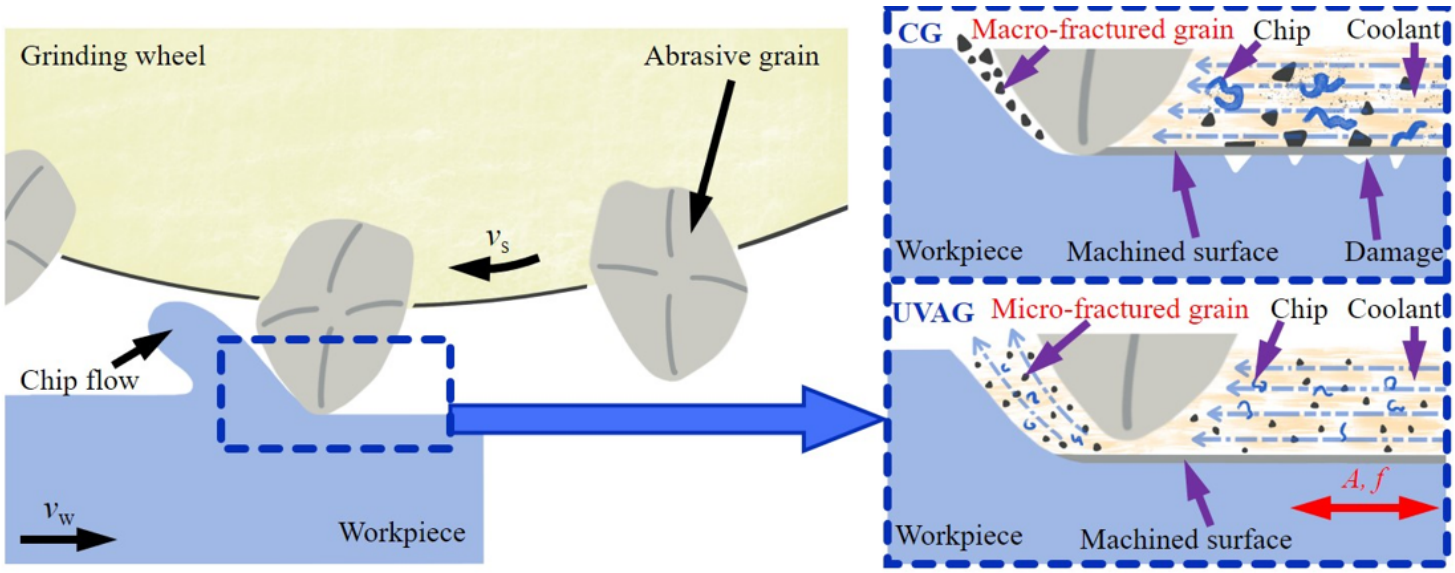

Figure 10

Schematic of grinding surface generation for CG and UVAG.